FINAL RESULTS FROM THE BIMA CMB ANISOTROPY SURVEY AND SEARCH FOR SIGNATURE OF THE SZ EFFECT

K.S. Dawson[1], W.L. Holzapfel[1], J.E. Carlstrom[2,3],
M. Joy[4], and S.J. LaRoque[2]
Submitted to Astrophysical Journal

ABSTRACT

We report the final results of our study of the cosmic microwave background (CMB) with the BIMA array. Over 1000 hours of observation were dedicated to this project exploring CMB anisotropy on scales between $1'$ and $2'$ in eighteen $6'.6$ FWHM fields. In the analysis of the CMB power spectrum, the visibility data is divided into two bins corresponding to different angular scales. Modeling the observed excess power as a flat band of average multipole $\ell_{eff} = 5237$, we find $\Delta T_1^2 = 220^{+140}_{-120}\,\mu\text{K}^2$ at 68% confidence and $\Delta T_1^2 > 0\,\mu\text{K}^2$ with 94.7% confidence. In a second band with average multipole of $\ell_{eff} = 8748$, we find ΔT_2^2 consistent with zero, and an upper limit $880\,\mu\text{K}^2$ at 95% confidence. An extensive series of tests and supplemental observations with the VLA provide strong evidence against systematic errors or radio point sources being the source of the observed excess power. The dominant source of anisotropy on these scales is expected to arise from the Sunyaev-Zel'dovich (SZ) effect in a population of distant galaxy clusters. If the excess power is due to the SZ effect, we can place constraints on the normalization of the matter power spectrum $\sigma_8 = 1.03^{+0.20}_{-0.29}$ at 68% confidence. The distribution of pixel fluxes in the BIMA images are found to be consistent with simulated observations of the expected SZ background and rule out instrumental noise or radio sources as the source of the observed excess power with similar confidence to the detection of excess power. Follow-up optical observations to search for galaxy over-densities anti-correlated with flux in the BIMA images, as might be expected from the SZ effect, proved to be inconclusive.

Subject headings: cosmology: observation – cosmic microwave background – Sunyaev-Zel'dovich effect

1. INTRODUCTION

The angular power spectrum of the Cosmic Microwave Background (CMB) has been measured with high signal to noise on scales from degrees to several arcminutes (e.g., Hinshaw et al. 2003, Kuo et al. 2004, Mason et al. 2003). However, observations of CMB anisotropy on arcminute scales, where secondary anisotropies such as the Sunyaev-Zel'dovich (SZ) effect (Sunyaev & Zel'dovich 1970) are expected to dominate the primary CMB anisotropy (e.g., Gnedin & Jaffe 2001), have not yet achieved comparable precision. At these finer angular scales, observations distant SZ clusters have the potential to be a powerful probe of the growth of structure in the Universe (Carlstrom, Holder, & Reese 2002). However, the power spectrum of the arcminute fluctuations reveals little information about the nature of the sources responsible for the anisotropy. As suggested by Rubino-Martin & Sunyaev (2003), higher order statistics of images can, in principle, be used to identify the unique signature of the SZ effect.

Beginning in the summer of 1998, we began a program to search for arcminute-scale CMB anisotropy using the Berkeley-Illinois-Maryland Association (BIMA[5])

interferometer. Initial results are included in earlier publications (Holzapfel et al. 2000, Dawson et al. 2001, and Dawson et al. 2002 (hereafter D2002)). A detailed description of the BIMA analysis, results from other experiments, and a comparison with theoretical models and simulations of structure formation can be found in D2002. In this paper, we report the final results from the BIMA CMB anisotropy survey. We describe the observations of the final fields in summer 2002 with the BIMA array and the Very Large Array (VLA[6]) in §2. The results of the power spectrum analysis, including a discussion of tests for systematic errors in the analysis are presented in §3. In §4 we examine the BIMA image statistics in order to constrain the origin of the observed anisotropy. In §5, we describe the results of follow-up optical observations used in an attempt to identify galaxy clusters in the BIMA fields. Finally, in §6, we summarize the results and present our conclusions.

2. OBSERVATIONS

The BIMA anisotropy survey consists of 18 fields that had not been previously observed for SZ galaxy clusters or CMB anisotropy at arcminute angular scales. Each field was observed with the BIMA array at a frequency of 28.5 GHz and the VLA at a frequency of 4.8 GHz. Analysis of ten fields observed with the BIMA array during the summers of 1998, 2000, and 2001 revealed evidence for a detection of power in excess of the instrument noise. A description of the analysis and results for the first ten

[1] Department of Physics, University of California, Berkeley CA 94720 (KD now at LBNL)
[2] Kavli Institute for Cosmological Physics, Department of Astronomy and Astrophysics, University of Chicago, Chicago IL 60637
[3] Department of Physics, Enrico Fermi Institute, University of Chicago, Chicago, IL 60637
[4] Department of Space Science, XD12, NASA Marshall Space Flight Center, Huntsville AL 35812
Electronic address: kdawson@lbl.gov
[5] The BIMA array is operated with support from the National

fields in the survey can be found in D2002. Eight new fields were added to the survey in the summer of 2002.

2.1. BIMA Observations

All anisotropy observations were made using the BIMA array at Hat Creek. Nine 6.1 meter telescopes of the array were equipped for operation at 28.5 GHz, providing a 6.6′ FWHM field of view. The first ten fields, BDF4-BDF13, were chosen to lie in regions expected to have minimal radio point source and dust contamination. The eight fields added in 2002, BDF14-BDF21, were chosen to lie two minutes east in Right Ascension of existing fields in the survey. Observations of these fields added another 489 hours of observations to the previously published data, for a total of 1096 hours for the complete BIMA survey. Each of these new fields was observed using the same phase calibrator as its previously observed nearest neighbor and analyzed following the data reduction as described in D2002. These fields were chosen to check for possible contamination of the signal correlated with telescope position. This makes for a total of 18 independent fields in the survey, covering approximately 0.2 square degrees. The pointing center, dates of observation, and observation time for each of the fields are given in Table 1. We dedicated $55 - 65$ hours of observation with the BIMA array to each of the new fields in order to achieve a uniform RMS noise level of $< 150 \,\mu$Jy/beam on short baselines (u-$v < 1.1 \,$kλ) for the entire sample. This noise level corresponds to an RMS of $15.55 \,\mu$K for a 2′ synthesized beam.

2.2. VLA Observations

To help constrain the contribution from point sources to the anisotropy measurements, we used the VLA at a frequency of 4.8 GHz to observe each field in the survey. With 1.5 hours per field, these observations yielded an RMS flux of $\sim 25 \,\mu$Jy/beam over a 9′ FWHM region with the same pointing center as a BIMA field. The positions of all point sources detected with significance $> 6\sigma$ within 400″ of the pointing center have been recorded. Measured point sources with fluxes corrected for attenuation by the primary beam at 4.8 GHz are listed in Tables 2 and 3.

If the spectra of the point sources are nearly flat or falling, deep observations with the VLA will identify those that lie near the noise level in the 28.5 GHz maps. However, it is possible that a radio source with a steeply inverted spectrum may lie below the VLA detection threshold but would still contribute significantly at 28.5 GHz. Advection dominated accretion flows are thought to be the most common inverted spectrum sources. They typically have a slowly rising spectrum, with a spectral index of 0.3 to 0.4 (Perna & DiMatteo, 2000) where the point source flux $S \propto \nu^{\alpha}$. Such a shallow spectrum would only provide a factor of two increase in flux between 4.8 GHz and 28.5 GHz; any source not seen with the VLA would be near the noise level of the BIMA observations.

To search for point sources with more steeply inverted spectral indices, we made VLA observations at 8.0 GHz of the five BIMA fields that most strongly indicate an excess of anisotropy power. If radio sources are the dominant contribution to the observed excess power, it is these fields that are the most likely to be contaminated. Results of these observations are found in Table 2 and

Table 3. The 8 GHz observations reached a RMS flux density of $20 \,\mu$Jy/beam at the center of the 5′ FWHM primary beam. Six of the 13 sources identified in the 4.8 GHz maps were detected in the 8.0 GHz maps with Signal-to-Noise ratio (SNR) > 3. The mean spectral index of the detected sources is found to be $\alpha = -0.4$. The fluxes of the other seven sources were poorly constrained because those sources were either too dim or were positioned outside of the 8.0 GHz primary beam where the instrument is most sensitive. The 8 GHz images produced no additional point source detections with SNR > 6, providing additional evidence against contamination by a population of radio sources with inverted spectra.

TABLE 1: Field Positions and Observation Times

Fields	R. A. (J2000)	Decl. (J2000)	Observation year(s)	Time (Hrs)
BDF4	$00^h\,28^m\,04.4^s$	$+28°\,23'\,06''$	98	77.6
HDF	$12^h\,36^m\,49.4^s$	$+62°\,12'\,58''$	98, 01	59.9
BDF6	$18^h\,21^m\,00.0^s$	$+59°\,15'\,00''$	98, 00	81.2
BDF7	$06^h\,58^m\,45.0^s$	$+55°\,17'\,00''$	98, 00	68.2
BDF8	$00^h\,17^m\,30.0^s$	$+29°\,00'\,00''$	00, 01	53.3
BDF9	$12^h\,50^m\,15.0^s$	$+56°\,52'\,30''$	00, 01	53.9
BDF10	$18^h\,12^m\,37.2^s$	$+58°\,32'\,00''$	00, 01	53.3
BDF11	$06^h\,58^m\,00.0^s$	$+54°\,24'\,00''$	00, 01	50.0
BDF12	$06^h\,57^m\,38.0^s$	$+55°\,32'\,00''$	01	54.8
BDF13	$22^h\,22^m\,45.0^s$	$+36°\,37'\,00''$	01	54.5
BDF14	$00^h\,26^m\,04.4^s$	$+28°\,23'\,06''$	02	62.4
BDF15	$06^h\,56^m\,45.0^s$	$+55°\,17'\,00''$	02	64.2
BDF16	$12^h\,34^m\,49.4^s$	$+62°\,12'\,58''$	02	64.5
BDF17	$18^h\,19^m\,00.0^s$	$+59°\,15'\,00''$	02	64.5
BDF18	$00^h\,15^m\,30.0^s$	$+29°\,00'\,00''$	02	57.8
BDF19	$06^h\,55^m\,38.0^s$	$+55°\,32'\,00''$	02	59.4
BDF20	$12^h\,48^m\,15.0^s$	$+56°\,52'\,30''$	02	54.7
BDF21	$18^h\,10^m\,37.2^s$	$+58°\,32'\,00''$	02	62.0

TABLE 2: Point Sources and Fluxes Identified from VLA Observations(1998-2001)

Field	Δ R.A. ($''$)	Δ DEC ($''$)	4.8 GHz (μJy)	8 GHz (μJy)	30 GHz (μJy)
BDF4	-96.8	255.7	1230 ± 90.6		
BDF4	72.8	178.2	514 ± 54.9		468 ± 313
BDF4	99.9	-89.4	221 ± 42.3		90.7 ± 225
BDF4	-94.9	268.4	391 ± 89.3		
HDF	-35.0	-85.0	832 ± 56.3		535 ± 185
HDF	255.0	-89.8	1380 ± 93.0		
HDF	178.3	-274.0	1520 ± 112		
HDF	222.5	-86.8	709 ± 64.6		
HDF	69.1	334.1	1120 ± 107		
HDF	-21.1	66.1	190 ± 36.2		
BDF6	-136.5	-283.5	592 ± 74.5	-51.3 ± 226	
BDF7	314.6	47.4	1554 ± 80.5		
BDF7	173.8	97.8	373 ± 40.1		156 ± 306
BDF7	253.8	-1.1	284 ± 49.5		
BDF8	-145.9	-266.1	1381 ± 94.1		
BDF8	27.6	280.9	611 ± 72.8		
BDF8	302.9	-79.5	622 ± 86.1		
BDF9	-221.9	-123.7	1500 ± 78.4		
BDF9	-192.7	215.8	1193 ± 81.3		
BDF9	245.2	-101.0	1039 ± 67.8		
BDF10	-158.5	-165.6	1670 ± 63.9		1610 ± 347
BDF10	-146.1	-183.9	320 ± 44.4		
BDF11	87.7	77.9	246 ± 34.6		
BDF11	342.8	8.8	865 ± 101		387 ± 179
BDF11	42.5	-11.8	152 ± 30.7		
BDF12	-241.0	-256.7	1620 ± 105	-97.4 ± 368	
BDF12	260.2	300.5	1191 ± 129	-1080 ± 905	
BDF12	-137.4	-133.4	278 ± 40.5	126 ± 36.7	165 ± 273
BDF12	170.9	66.7	211 ± 38.7	98.8 ± 33.9	-151 ± 259
BDF13	181.4	-49.5	721 ± 51.2	531 ± 50.8	935 ± 271
BDF13	-154.0	299.7	1145 ± 98.8	126 ± 427	
BDF13	225.1	-99.9	317 ± 56.4	11.4 ± 106	

Entries are left blank for fields not observed at 8 GHz. For the 30 GHz BIMA observations, entries are blank for those point sources which lie outside the primary beam and are not detected at $> 3\sigma$ significance.

TABLE 3: Point Sources and Fluxes Identified from VLA Observations(2002)

Field	Δ R.A. ($''$)	Δ DEC. ($''$)	4.8 GHz (μJy)	8 GHz (μJy)	30 GHz (μJy)
BDF14	125.1	-166.8	1186 ± 35.3	1235 ± 63.1	
BDF14	-56.3	30.3	226 ± 24.1	295 ± 22.2	-195 ± 143
BDF14	17.6	-183.4	578 ± 26.5	367 ± 48.9	110 ± 244
BDF15	-6.9	-324.4	9390 ± 78.6		6390 ± 857
BDF15	-129.0	218.7	637 ± 42.1		
BDF15	77.4	-282.6	707 ± 51.4		
BDF16	-157.8	116.7	1091 ± 38.3		212 ± 274
BDF16	-266.2	198.5	2553 ± 74.8		
BDF16	-158.4	33.6	576 ± 33.1		215 ± 222
BDF17	39.9	169.3	431 ± 26.2	774 ± 44.4	694 ± 228
BDF18	-213.4	381.6	6902 ± 145		
BDF18	-106.1	-0.7	465 ± 25.7		145 ± 168
BDF18	285.4	2.8	988 ± 49.9		
BDF18	137.7	93.9	515 ± 29.7		103 ± 222
BDF18	-9.5	290.3	1636 ± 50.5		
BDF18	112.9	165.9	266 ± 32.8		381 ± 276
BDF18	-32.2	105.4	333 ± 25.5		142 ± 170
BDF19	31.9	169.4	289 ± 32.8		-95 ± 237
BDF19	-169.8	-17.3	363 ± 32.6		-16 ± 234
BDF19	-128.7	-76.5	403 ± 30.4		167 ± 210
BDF20	245.8	15.9	3809 ± 49.4		1240 ± 400
BDF20	-131.5	394.5	4957 ± 136		
BDF20	89.7	360.3	3272 ± 96.6		
BDF20	-301.9	149.2	2851 ± 76.0		
BDF21	277.3	-180.0	2103 ± 57.5		
BDF21	229.4	74.1	1187 ± 34.8		
BDF21	-315.9	-224.9	838 ± 82.2		
BDF21	115.7	268.9	470 ± 44.2		

Entries are left blank for fields not observed at 8 GHz. For the 30 GHz BIMA observations, entries are blank for those point sources which lie outside the primary beam and are not detected at $> 3\sigma$ significance.

Dawson et al.

3. EXCESS POWER ESTIMATE

Following the method of D2002, the excess power in the BIMA data is computed assuming that the angular power spectrum can be described by either one or two flat band powers. Point sources identified with the VLA are tabulated in §2.2 and are removed from the data using the constraint matrix technique described in D2002. Confidence intervals for the band powers are determined using the integrated likelihood also described in D2002. In Table 4, we show the most likely ΔT^2 and approximate uncertainty computed from visibilities in the $0.63-1.1\,\mathrm{k}\lambda$ range for each of the 18 fields in the survey. Results for the complete data set are included in Table 5 for the cases when the power spectrum is modeled by two bandpowers corresponding to u-v ranges $0.63-1.1\,\mathrm{k}\lambda$ and $1.1-1.7\,\mathrm{k}\lambda$, and for a single bin covering the range $0.63-1.7\,\mathrm{k}\lambda$.

In the combined analysis of all 18 fields, we allow for $\Delta T^2 < 0.0$ in determining the most likely estimate of measured power and confidence intervals. Excess power corresponding to $\Delta T_1^2 > 0$, was observed with 94.7% confidence in the $0.63-1.1\,\mathrm{k}\lambda$ bin. In the u-v range $1.1-1.7\,\mathrm{k}\lambda$, the level of observed power was consistent with zero and we found an upper limit $\Delta T_2^2 < 880\mu\mathrm{K}^2$ at 95% confidence. When an analysis is performed combining all data into a single bin, we find an estimate of excess power excluding zero, $\Delta T^2 > 92.3\%$ confidence.

Window functions for each of these bands are produced from the noise weighted sum of the window functions for the individual visibilities. Averaged over all 18 fields, the $0.63-1.1\,\mathrm{k}\lambda$ band has an average value of $\ell_{eff} = 5237$ with FWHM $\ell = 2870$. The window function for visibilities in the u-v range $1.1-1.7\,\mathrm{k}\lambda$ has an average value $\ell_{eff} = 8748$ with FWHM $\ell = 4150$. For the single band model covering the u-v range $0.63-1.7\,\mathrm{k}\lambda$, the window function has an average value $\ell_{eff} = 6864$ with FWHM $\ell = 6800$.

TABLE 4: Power Estimates for $0.63 - 1.1\,\mathrm{k}\lambda$

	$\Delta T^2(\mu\mathrm{K}^2)$	
Field	Most Likely	σ
BDF4	0.0	600
HDF	0.0	270
BDF6	380	455
BDF7	300	1050
BDF8	0.0	390
BDF9	0.0	590
BDF10	0.0	360
BDF11	50	920
BDF12	1590	1165
BDF13	1480	1260
BDF14	690	920
BDF15	0.0	660
BDF16	300	880
BDF17	1390	1400
BDF18	200	990
BDF19	0.0	900
BDF20	290	910
BDF21	0.0	310

The likelihood distribution near the maximum ($\Delta T_B^2 = \overline{\Delta T^2}_B$) for the data defined by bin B is well described by a offset log-normal function (Bond, Jaffe, & Knox, 2000),

$$\ln\mathcal{L}(\mathbf{\Delta T^2}) = \ln\mathcal{L}(\overline{\mathbf{\Delta T^2}}) - \frac{1}{2}\sum_B \frac{(Z_B - \overline{Z}_B)^2}{\sigma_B^2}e^{2\overline{Z}_B}, \tag{1}$$

where the offset log-normal parameters $\mathbf{Z}$ are defined as

$$Z_B = \ln{(\Delta T_B^2 + x_B)}. \tag{2}$$

The likelihood functions are fit with this model to determine values for the curvature at peak σ_B, which represents the uncertainty in the measurement, and log-normal offset x_B to the likelihood functions reported in Table 5.

3.1. Point Source Removal

As discussed in §2.2, we have adopted a detection threshold of 6σ for identifying point sources in the VLA data. We measured the effect of eight different point source detection thresholds on the measured excess power from the combined analysis of the 18 fields. We choose point source detection limits in terms of SNR rather than flux to account for attenuation by the VLA primary beam. The noise is assumed to have an RMS of $25\,\mu\mathrm{Jy/beam}$ in all VLA fields. The results are listed in Table 6.

In the case for which no point sources are removed, the most likely value of $\Delta T_1^2 = 430\,\mu\mathrm{K}^2$ appears significantly elevated due to contamination by radio point sources. The measured excess power drops from $430\,\mu\mathrm{K}^2$ in the case of no point source constraints to a broad minimum of $\sim 200 - 250\,\mu\mathrm{K}^2$ for removal of sources detected with less than 8σ significance. As the detection threshold decreases, the removal of point sources will begin to remove a significant number of degrees of freedom from the analysis, resulting in increased uncertainty in the measurement of power. For example, a detection threshold for point sources of 4σ removes three times as many sources from the data as a detection threshold of $8 - 12\sigma$. The uncertainty in the measurement begins to significantly increase with a point source detection threshold less than 6σ while the subtraction of the additional sources have no effect on the observed excess power. Therefore, we adopt 6σ as the point source detection threshold.

While the contribution to anisotropy from point sources is expected to scale as ℓ^2, the estimate of excess power is consistent with zero on finer angular scales as shown in Table 5. It should also be noted that no additional point sources were found in the 8 GHz VLA observations. These observations reinforce the conclusion that the contribution of point sources to the observed excess power is well constrained in the power spectrum analysis.

3.2. Systematic Tests

We performed tests for systematic errors in all fields identified as having significant excess power. This analysis was limited to visibility data in the u-v range $0.63-1.1\,\mathrm{k}\lambda$ described by ΔT_1^2 where the most significant detection of excess power occurs. The modeled power in the second bin is fixed at $\Delta T_2^2 = 0$ for all tests described in this section. We searched for systematic errors by repeating the power spectrum analysis after splitting the

TABLE 5: Power Estimates for Combined Data Sets

	$\Delta T^2 (\mu K^2)$				Likelihood
u-v range	Most Likely	68% Confidence	σ_B	x_B	$\Delta T^2 > 0$
$0.63 - 1.1\,\mathrm{k}\lambda$	220	$100 - 360$	130	625	94.7%
$1.1 - 1.7\,\mathrm{k}\lambda$	-40	< 420	395	3040	
$0.63 - 1.7\,\mathrm{k}\lambda$	170	$70 - 290$	110	490	92.3%

TABLE 6: Effect of Point Source Model on ΔT_1^2

		$\Delta T_1^2 (\mu K^2)$	
VLA Detection Limit (SNR)	Number of Sources	Most likely	σ
none	0	430	155
> 40	7	350	150
> 20	27	290	140
> 12	45	260	130
> 8	58	240	135
> 6	62	220	130
> 5	98	210	135
> 4	168	250	150

data into a number of subsets. The first set of tests was designed to search for systematic contamination that changes with time. Relative to a source on the celestial sphere, terrestrial sources will appear to move rapidly over the course of a single observation, while the sun or moon will vary in position by many degrees over the course of a typical month long observation. We searched for such signals by analyzing the data after dividing it into subsets corresponding to the first, second, and third sections of both observation tracks and the period of observation. For the field BDF6, the only field observed in multiple years that was found to have a significant level of excess power, we also compared the results of observations taken in 1998 and 2000. Instrumental effects that manifest themselves as spurious signals on a given telescope or baseline are also a potential source of systematic error. We searched for such effects by breaking the data into subsets of four and five telescopes and looking for antenna based systematic errors. For a test of baseline based systematic errors, we created east-west and north-south baseline subsets. The different data and instrument subsets used in the search for systematic errors are listed in Table 7. The results for the application of these tests applied to fields BDF6, BDF12, BDF13, BDF14, and BDF17 are shown in Figure 1.

TABLE 7: Cuts Used in Systematic Tests

| Test Number	Data Subset
1	First Four Hours UT
2	Middle Three Hours UT
3	Final Four Hours UT
4	First Third of Observation Dates
5	Middle Third of Observation Dates
6	Final Third of Observation Dates
7	Baselines from Subarray of four Telescopes
8	Baselines from Subarray of five Telescopes
9	East-West Baselines
10	North-South Baselines
11	First Year of Observation (BDF6 only)
12	Second Year of Observation (BDF6 only)

Dawson et al.
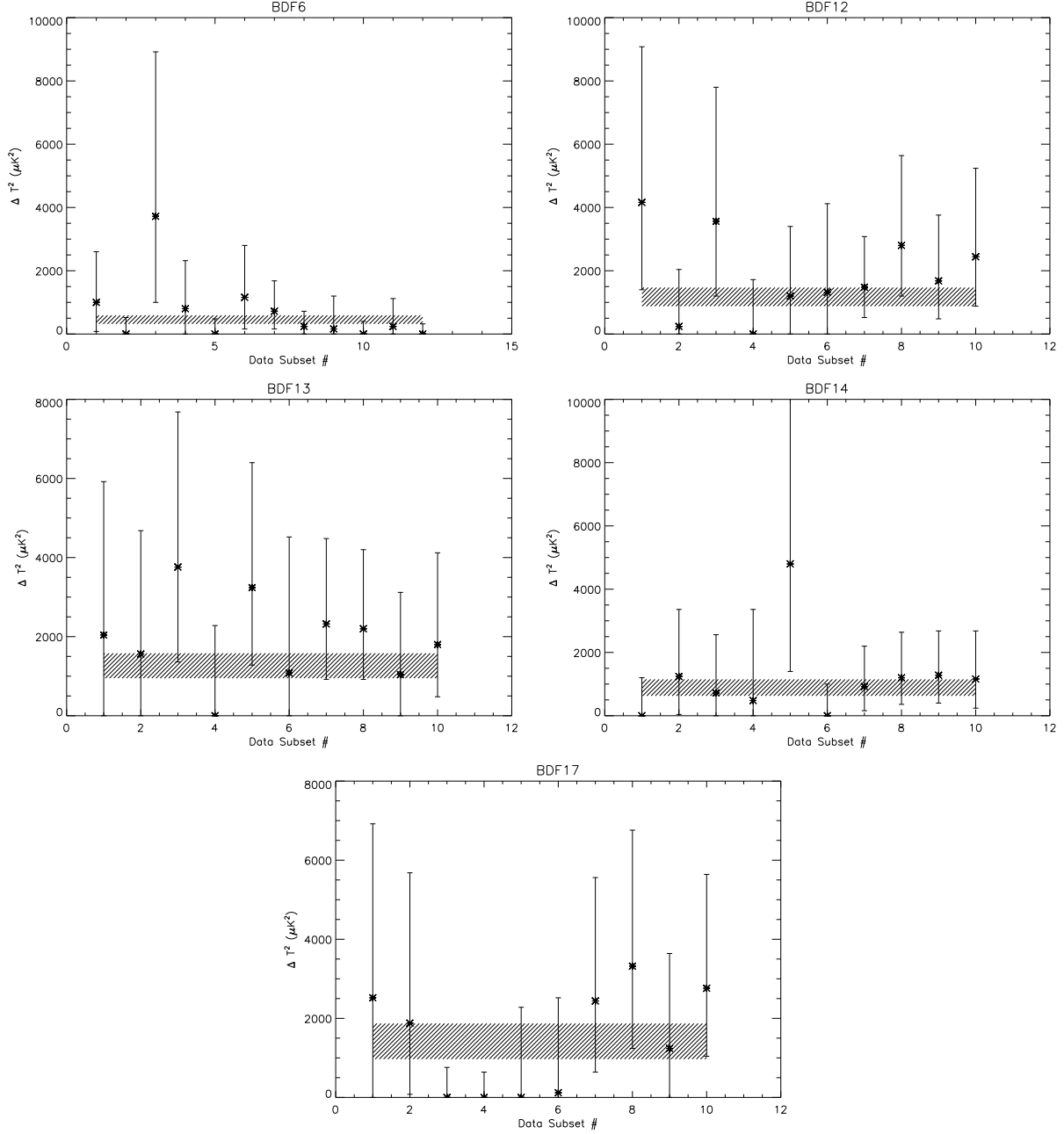
FIG. 1.—: Band power estimates and confidence intervals for each systematic test in those fields found to have significant levels of excess power. The shaded region represents the 68% confidence intervals for the full data set of each field.

If a systematic error was associated with one of these subsets, then the level of excess power in that subset should increase. However, as can be seen in Figure 1, we found approximately the same level of excess power in each subset. Of the fifty-two subsets, only the final four hours of UT in BDF6 (third data point in Figure 1) and the middle third of observation dates for BDF14 (fifth data point in Figure 1) are found to have estimates of excess power and 68% confidence intervals that lie above the 68% confidence limits of the full analysis. Therefore, we consider these two subsets to be the most likely to be systematically biased. To test the possible contribution from systematic errors in these subsets to the measured excess power, we repeated the analysis on the 18 combined fields after removing these two subsets. We found an estimate of $\Delta T^2 = 180^{+140}_{-120} \mu K^2$, not significantly different than the reported value of $\Delta T^2 = 220^{+140}_{-120} \mu K^2$ for the entire survey.

3.3. Correlated Signal Between Independent Fields

It is possible that a hardware malfunction could create a systematic false correlation that is constant or changes slowly with sky position. To test for this, we combined the raw visibilities from observations of all fields taken in a single summer, as if all the data came from a single pointing. If the fields contain random noise or independent sky signal, the power in the combined fields should decrease significantly when the visibilities are averaged. A false detection caused by correlations introduced in the hardware or other local effects might, depending on its stability, enhance the excess power in the anisotropy measurement when the independent observations are combined. The results of the analysis of the combined data sets, listed in Table 8, are consistent with instrumental noise at 68% confidence, as expected for non-correlated independent observations.

To test for false correlations that vary slowly across the sky, we observed a set of fields offset by $2'$ in RA from fields that had been previously observed. The fields BDF6, BDF12, BDF13, BDF14, and BDF17 have the most significant levels of excess power of the individual fields in the survey. We have neighboring fields for all of these except for BDF13. The raw visibilities of the neighboring fields were combined and then analyzed for excess power; the results of this analysis are shown in Table 8. In all cases, the observed anisotropy power decreases as we would expect for the combination of visibilities from independent patches of sky. Therefore, we conclude that there does not appear to be any false correlation that is constant or slowly varying with sky position. In addition, there does not appear to be any correlation between excess power and proximity to the sun, none of the fields analyzed for systematic error were near the sun's location of $11 - 12$ hr R.A. during the summer months. Overall, we find no evidence that our results are biased by systematic effects or astrophysical contamination.

3.4. Constraints on σ_8

As was described in the introduction, the most likely astrophysical source of the excess power observed in the survey is expected to be CMB anisotropy arising from the SZ effect in clusters of galaxies. Assuming that the observed excess power is entirely due to the SZ effect, we

TABLE 8: Results of Combining Independent Observations

Dataset	$\Delta T_1^2 (\mu K^2)$ Most likely	σ
1998 data	60	220
2000 data	0	220
2001 data	40	180
2002 data	0	40
BDF12	1590	1165
BDF19	0.0	900
BDF12/2+BDF19/2	560	740
BDF6	380	1050
BDF17	1390	1400
BDF6/2+BDF17/2	640	580
BDF4	0	600
BDF14	690	920
BDF4/2+BDF14/2	120	220

use a publicly available archive of N-body simulations [7] (Schulz & White, 2003) to add the expected signal from the SZ effect to Monte Carlo noise realizations. These simulations predict the evolution of mass from $z = 60$ to present in a cosmological model described by $\Omega_M = 0.3$, $\Omega_\Lambda = 0.7$, $\Omega_b h^2 = 0.02$, $h = 0.7$, $n = 1$ and $\sigma_8 = 1.0$. Only dark matter is included in these simulations, and the baryons contributing to the SZ signal are added assuming that the gas closely traces the dark matter. Independent regions of the N-body simulations are multiplied by the $6.6'$ FWHM primary beam and transformed into the u-v plane with the same u-v sampling as the real BIMA data. Noise is added to each u-v point with a variance determined from the observed visibilities. Therefore, each simulated observation has u-v coverage and noise characteristics identical to the real BIMA observation of each field. The analysis of one hundred realizations of the BIMA survey with unique instrumental noise and simulated SZ sky resulted in an excess power of $\Delta T^2 = 216 \pm 190 \mu K^2$ at 68% confidence; this is remarkably close to the level of excess power found in the BIMA survey.

Komatsu and Seljak (2002) demonstrate that the amplitude of the SZ power spectrum has a strong dependence on σ_8, with $\Delta T^2 \propto \sigma_8^7$ for σ_8 near unity. We scale the simulated SZ images by $\sigma_8^{7/2}$ to produce skies corresponding to different values of σ_8. These images are transformed to the $u - v$ plane, combined with the simulated instrumental noise, and used to compute the likelihood of each value of σ_8 resulting in the observed excess power, which we approximate as $\Delta T_1^2 = 180 - 260 \mu K^2$. The relative likelihood that simulations with a given value of σ_8 will reproduce the observed excess power is determined from 10,000 realizations of the BIMA survey with σ_8 ranging from 0.0 to 1.5 The resulting relative likelihood shown in Figure 2 includes contributions to the uncertainty from both noise in the measurement and sample variance due the non Gaussian nature of the SZ signal and the small patch of sky surveyed. Assuming an additional 10% uncertainty in the simulations (Ko-

---

[7] Data available at http://pac1.berkeley.edu/tSZ/

matsu & Seljak, 2002, Goldstein et al. , 2003), we find $\sigma_8 = 1.03^{+0.20}_{-0.29}$ at 68% confidence and $\sigma_8 = 1.03^{+0.30}_{-0.96}$ at 95% confidence.
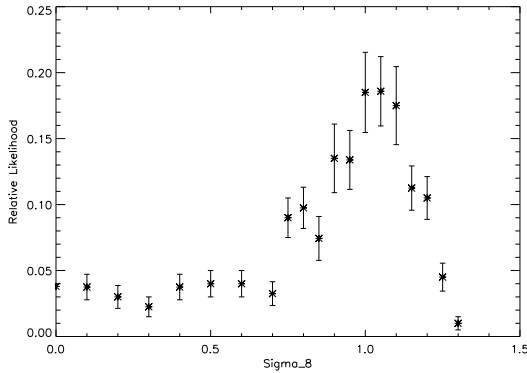

Fig. 2.—: Relative likelihood of measuring the observed excess power as a function of σ_8. The uncertainty at each point is determined by the Poisson statistics for the number of events in that bin.

4. IMAGE ANALYSIS

Analysis of the complete BIMA survey results in a detection of excess power with nearly 95% confidence. However, with the power spectrum analysis, we are unable to determine if the excess power is caused by sources with negative flux as would be expected from the SZ effect in galaxy clusters at 30 GHz. The statistics of the pixel flux values in the images contain additional information that can in principle constrain possible sources of the excess power.

Images are reconstructed directly from the visibility data for each field in the BIMA survey using the DIFMAP software package (Pearson et al. 1994). Positions determined from the VLA data are used to model and remove point sources ($> 6\sigma$) in the u-v plane using baselines with u-v radius $> 1.5\,\mathrm{k}\lambda$ ($\sim 50\%$ of the visibilities). BIMA fields are imaged at a resolution of $7.5''$ per pixel after applying a Gaussian taper with a half-power radius of $1.0\,\mathrm{k}\lambda$ to the visibility data to maximize brightness sensitivity. These mapping parameters are used when presenting images of bright SZ clusters observed with the BIMA array (i.e. Laroque et al. 2003) and produce a synthesized beam which is well matched to cluster scales. A map of a typical synthesized beam can be found in Figure 3. The response of the first negative sidelobe is a factor of four lower than response at the center of the beam.

The typical RMS noise is $110\,\mu\mathrm{Jy/beam}$ for an image with $90''$ FWHM synthesized beam. The RMS for each image listed in Table 9 are computed directly from the noise properties of the images. The RMS temperature estimates correspond to the synthesized beamsize computed for the u-v coverage of each experiment.

To provide a visual representation of the data used in the analysis, images of the BIMA fields are reproduced in Figure 4. The dashed circle in each image represents the radius at which the primary beam attenuates the sky signal by a factor of two relative to the pointing center. Regions lying far outside the primary beam can be used
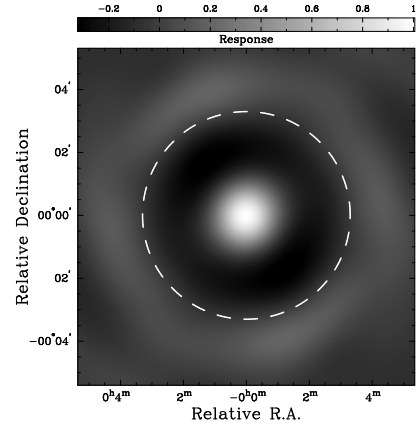

Fig. 3.—: Typical synthesized beam created from the u-v coverage used in the analysis of image statistics. The dotted line shows the half-power radius of the primary beam.

TABLE 9: Properties of Each Image Used in Analysis of Image Statistics

| Field	Synthesized Beamsize($''$)	RMS ($\mu\mathrm{Jy\,beam}^{-1}$)	RMS (μK)
BDF4	90.5×105.1	107.1	16.9
HDF	91.4×95.9	113.7	19.5
BDF6	90.7×97.5	92.4	15.7
BDF7	91.2×98.2	105.4	17.6
BDF8	87.9×90.4	109.9	20.7
BDF9	88.0×91.7	111.4	20.7
BDF10	88.0×90.3	109.4	20.7
BDF11	89.0×90.4	109.8	20.5
BDF12	88.7×92.0	112.3	20.6
BDF13	89.6×91.3	113.1	20.7
BDF14	86.6×89.9	106.9	20.6
BDF15	87.2×90.5	109.1	20.7
BDF16	87.4×91.5	108.7	20.4
BDF17	86.0×90.3	105.2	20.3
BDF18	86.3×91.7	107.7	20.4
BDF19	88.0×90.7	109.5	20.6
BDF20	86.8×91.6	108.4	20.4
BDF21	86.8×91.8	106.7	20.1

to compute the level of instrumental noise in the map.
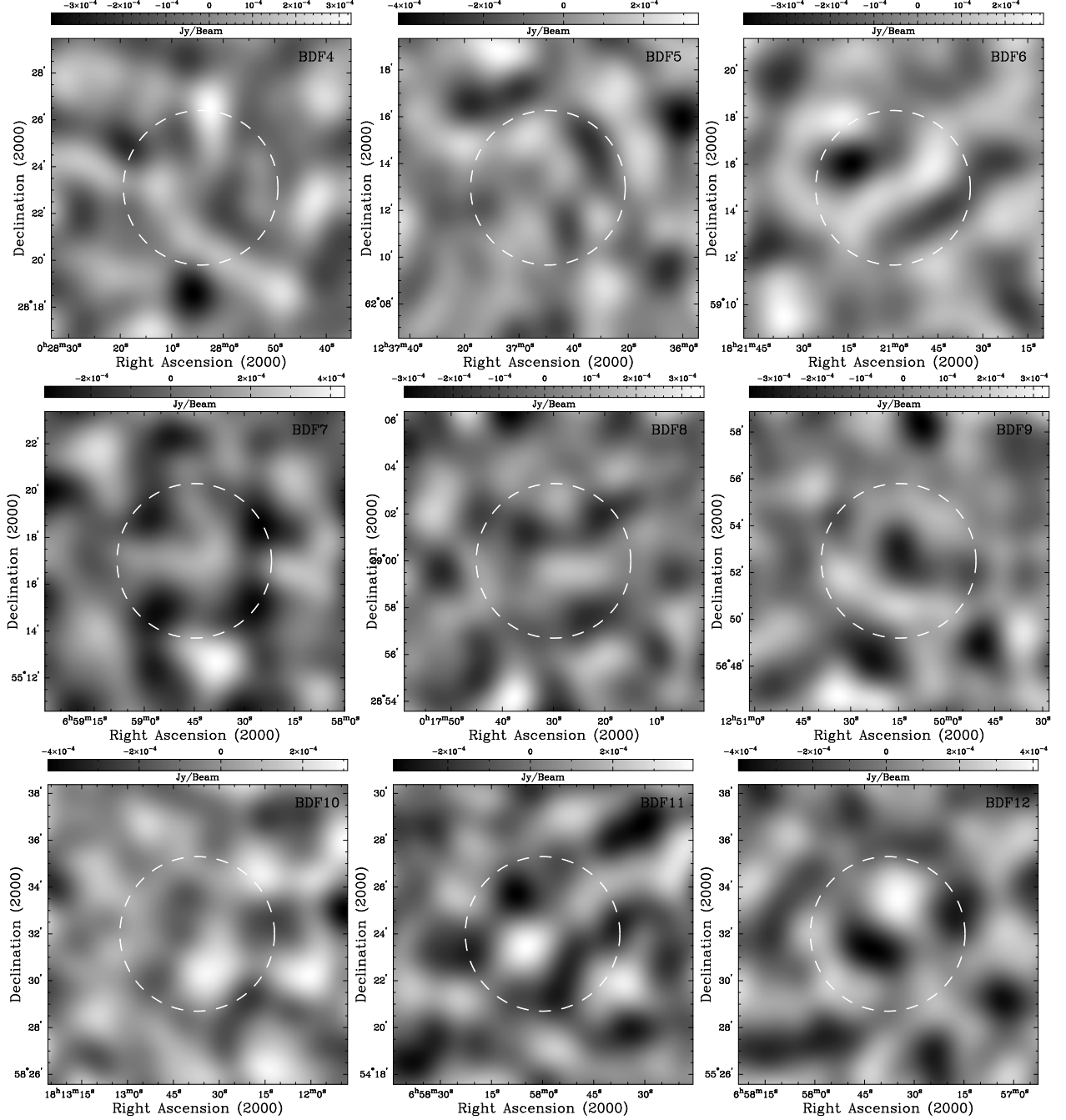
FIG. 4.—: BIMA Images after applying a Gaussian taper with a half-power radius of 1.0kλ to the visibility data. Point sources identified in the VLA images have been modeled from the long baselines (u-$v > 1.5$kλ) and removed directly from the visibility data. Dashed lines correspond to the half power radius of the primary beam.
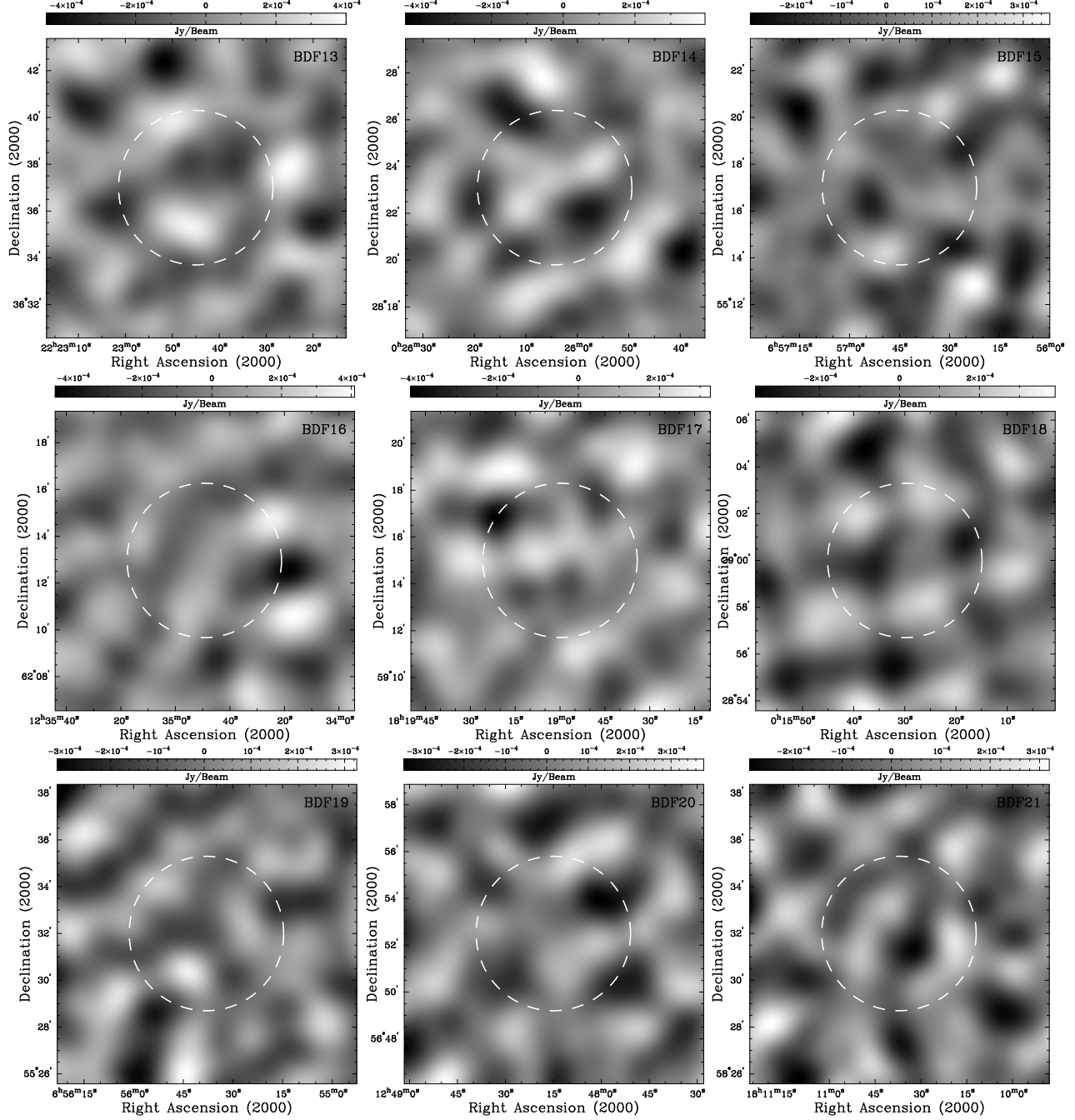
FIG. 4.—: Contd.

4.1. Image Simulations

Decrements caused by galaxy clusters would be expected to produce an excess of high SNR negative pixels. We attempt to detect this unique signature using higher order statistics of the image flux distribution as described in Rubino-Martin & Sunyaev, 2003. We compute asymmetry, skewness, and extrema in the observed data set. These results are compared to both simulations of instrumental noise and to simulations of SZ galaxy clusters added to instrumental noise in order to determine the significance of the observed distribution of flux.

The Fourier transform of the visibilities measured by the interferometer into the image plane introduces correlations between pixels which complicate the noise properties. In order to better understand this, we generated Monte Carlo simulations of the visibility data and transformed them into images. We created two sets of simulations, each containing 100 realizations of the full set of 18 images. These simulations are used to quantify the significance of applying the statistical tests to the BIMA images. The first set of simulations uses random complex visibilities with variances consistent with the observed noise for each image. At each point in u-v space in the observed data, a simulated visibility is created with a real and imaginary component from a random sampling of a Gaussian distribution with variance determined from the weight of that visibility. Therefore, each simulated observation has u-v coverage and noise characteristics identical to the real BIMA observation of each field.

In the second case, we add the expected contribution from the SZ sky to the MC noise realizations using the same simulated SZ sky images described in Section 3.4 with σ_8 fixed to 1.0. Independent regions of the N-body simulations are attenuated with the 6.6′ FWHM primary beam and transformed into the u-v plane using the exact same u-v sampling as that in the real BIMA data. Noise is then added to the visibility data in the same way as for the noise-only simulations and the data is then transformed into the image plane for analysis.

The image statistics of the observed images are compared with those generated from the Monte Carlo simulations. For each simulation, an image is generated from the raw visibilities tapered in the u-v plane with a $1.0\,\mathrm{k}\lambda$ FWHM Gaussian. Statistics are generated directly from the images of the 100 simulations. Using a large number of Monte Carlo simulations, one can produce a probability distribution for each observable statistic. The most likely value and integrated confidence intervals can be taken from this distribution and compared to the results of the real observations. Due to the modest number of 100 simulations of the survey, the shape of the pixel distribution is strongly dependent on bin size and bin spacing, leaving the most likely value as a poorly determined quantity. Instead, the median value in the 100 simulations is taken to be the most likely estimate. The terms defining the 16th and 84th percentile in the distribution are taken to be the lower and upper bounds to the 68% confidence intervals, respectively. The 4 nearest neighbors to the median, lower bound, and upper bound in the distribution are averaged to reduce the noise in the estimates.

We use a histogram of pixels binned in intervals of significance, $S = x_i/\sigma$, where x_i is the value at pixel i and σ is the estimated image RMS (approximately $110\,\mu\mathrm{Jy/beam}$). This is equivalent to weighting the pixels by the sensitivity of the observation. We can compare the pixel distributions for observed data and simulations by comparing the histogram of the images as shown in Figure 5.
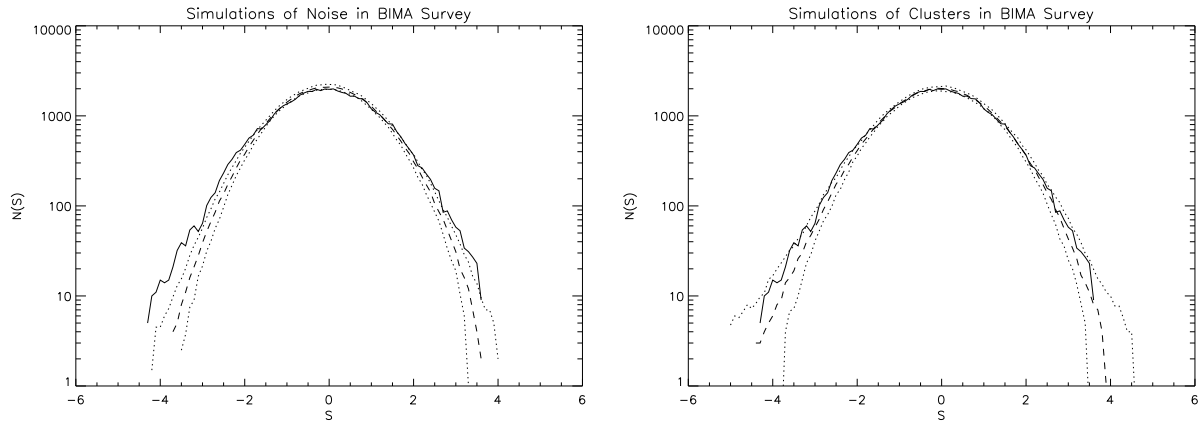
F<small>IG</small>. 5.—:
The figure on the left represents the histogram for simulations including only instrumental noise. The figure on the right represents the simulations with clusters added. In both cases, the solid line represents observed data, the dashed line represents the most likely value from the simulations, and the dotted lines represent the 68% confidence interval of the simulations. The simulations including clusters are a better fit to the observed data not only in the region of negative pixels, where the SZE is expected to directly contribute to the signal, but also in the region of positive pixels where the effects of the negative sidelobes contribute to the signal.

4.2. *Asymmetry of Pixel Distribution*

For a given image, we can characterize the pixel flux distribution by selecting a flux interval ΔD, and computing a histogram of the number of pixels with a flux between $D - \Delta D/2$ and $D + \Delta D/2$). The asymmetry of this histogram can be estimated directly as the difference in area between the positive and negative regions. A comparison of this statistic for the BIMA images and simulations is shown in Figure 6.
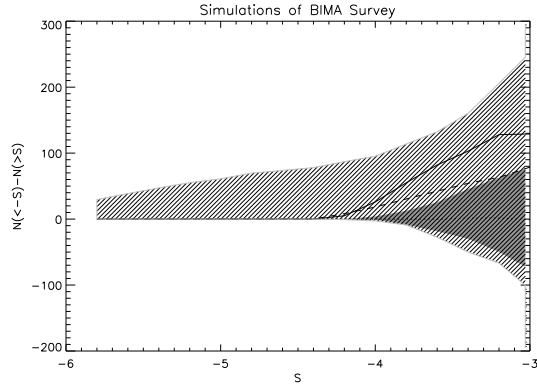
Fig. 6.—:
This figure describes the asymmetry of the pixel distribution as a function of SNR. The dark shaded region and dotted line represent the 68% confidence intervals and median asymmetry of the simulations that include only instrumental noise. The region of angled parallel lines and the dashed line represent the 68% confidence intervals and median asymmetry of simulations that also include the SZE. The black solid line represents the observed data.

It should be noted that the cluster simulations produce an excess of positive pixels compared to simulations of instrumental noise only. There are no sources with positive flux included in the cluster simulations, however pixels with positive flux are expected due to the sidelobes of the synthesized beam. A Gaussian taper was applied to the u-v data to minimize the sidelobes and this effect.

It is clear from Figure 6 that the observed data is consistent with the asymmetry in the simulations that include galaxy clusters and inconsistent with simulations that include only noise. For example, the excess of pixels with $S < -3$ in the observed data exceeds that in the simulations of instrumental noise at 86% confidence. The number of pixels with $S < -4$ exceeds that found in the simulations of only instrumental noise at 88% confidence. Therefore, the application of this statistic results in a detection of signal with the morphology of the SZ effect with a significance comparable to the significance of the detection of excess power reported in Section 3. In fact, the observed asymmetry in the BIMA data exceeds the mean value from the noise & SZ simulations.

As a simple exercise, a similar analysis is used to rule out positive flux (such as point sources) as the cause of excess power with slightly less confidence; we simply repeat the analysis described, but with the sign of the flux from clusters reversed. The excess of pixels with $S < -3$ in the observed data exceeds that in the simulations using positive flux at 74% confidence. The excess

of pixels with $S < -4$ exceeds that in simulations of instrumental noise at 76% confidence. A more rigorous analysis for point sources would include a more realistic distribution of point sources and take into account the details of their removal using the full, equally weighted, set of visibilities. This expanded analysis is considered unnecessary given the results of the VLA observations, constraints on point sources, and lack of power at finer angular scales. Nonetheless, this method would be useful in cases where rejection of point sources was less certain. We again conclude that it is very unlikely that point sources are responsible for the asymmetry observed in the BIMA image pixel fluxes.

4.3. *Skewness of Pixel Distribution*

A measure of skewness conveys information about the sign of the features producing the deviation from Gaussianity. This quantity can be estimated using the third moment of the data:

$$Y = \frac{1}{N_{pix}} \sum_{i=1}^{N_{pix}} (x_i - \overline{x})^3 \qquad (3)$$

The skewness of the data derived from the BIMA images is compared to the skewness determined from the Monte Carlo simulations in Figure 7.
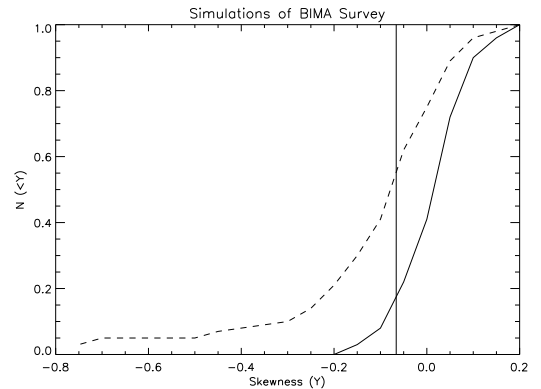

Fig. 7.—:
The cumulative count of simulations as a function of skewness. The solid line represents the model assuming only instrumental noise and the dashed line represents the model including the simulated SZ sky from the n-body simulations. The vertical line represents the skewness measured in the BIMA data.

Analysis of the simulations of instrumental noise alone results in a skewness of 0.01 ± 0.08 at 68% confidence, while the simulations of clusters plus instrumental noise give a mean skewness of $-0.096^{+0.11}_{-0.15}$. The skewness in the BIMA observations was found to be $Y = -0.066$, a value that is inconsistent with the noise only simulations at 64% confidence. Repeating the simple analysis described at the end of §4.2, the skewness is inconsistent with positive flux sources as the cause of the observed excess power at 84% confidence.

4.4. *Outliers in the Distribution*

In addition to the two tests described above, we performed simulations to characterize the significance of outliers in pixel flux distributions of the individual fields.

We identified the most negative pixels in each of the 18 BIMA fields and compared these with the results of the simulations. Seven BIMA fields were observed to have decrements with $S < -3\sigma$, more than occurred in 93% of the survey simulations with noise only. Two BIMA fields were observed to have decrements with $S < -4\sigma$, more than occurred 99% of the survey simulations including only noise. None of the observed BIMA fields had a pixel with positive flux $S > 4\sigma$.

4.5. *Interpretation of Image Statistics*

In each of the statistical tests described above, the BIMA images were found to be inconsistent with those produced by instrumental noise alone at approximately the $1-2\sigma$ level, comparable to the significance of the detection of excess power. Although the analysis does not conclusively determine the source of the excess power, the results are consistent with the signal expected from SZ galaxy clusters. The results are also inconsistent with radio point sources being the source of the observed excess power. Despite the lack of a definitive conclusion from these tests, the results are encouraging. In order to investigate what observations would be required to make a definitive measurement, we performed simulations of the 18 field survey with four times the observation time, or equivalently four times the correlation bandwidth. These simulations resulted in a detection of excess power and skewness at the 4σ level in more than 50% of the simulations. Such a detection would provide convincing evidence for SZ clusters as the source of excess power.

5. OPTICAL OBSERVATIONS OF BIMA FIELDS

To date, all known galaxy clusters have been discovered through optical or X-ray observations. A negative correlation of the observed fine scale CMB anisotropy with X-ray or optical emission would be a smoking gun for the discovery of a cluster through the SZ effect. To search for this correlation, we observed ten of the BIMA fields using ground-based optical telescopes. We selected the five fields with significant levels of excess power assuming that they are the most likely candidates for identifying galaxy clusters. In addition to those five fields, we observed five BIMA fields that lie at convenient RA during the nights we were awarded time. Imaging was performed using I and R filters on the LRIS instrument (Oke et al. 1995) on the 10 m Keck[8] I telescope. Imaging in z' was done with the MOSAIC instrument (Wolfe et al. 1998) on the 4m Kitt Peak National Observatory telescope[9].

We performed an analysis of the optical images using a method similar to that used in the Red Cluster Survey (RCS) survey (Gladders & Yee, 2000). We first categorized objects into two redshift bins determined by color $R - I$ and $R - z'$. The first bin contains only high redshift galaxy candidates. These candidates have color $R - I > 1.0$ and $R - z' > 1.0$, implying a red sequence redshift $0.5 < z < 1.0$. The second bin contains low redshift galaxy candidates. These candidates have color $0.0 < R - I < 1.0$ and $0.0 < R - z' < 1.0$ implying a redshift $z < 0.5$. All objects not satisfying these criteria are considered foreground contamination and are discarded. An exponential kernel is used to smooth the maps of detected objects in each redshift bin with scale radius of $20''$ to create a surface density map. We then create a product map by simply multiplying each surface density map with the corresponding BIMA map described in §4. The product maps are searched for peaks and asymmetry in the distribution. Statistics are quantified with Monte Carlo simulations of random BIMA fields. The resulting analysis (described in full detail in Dawson, 2004) showed no significant correlation between overdensities of galaxies in the optical maps and decrements of flux in the BIMA 28.5 GHz maps.

While the follow-up optical observations do not confirm the hypothesis that the observed anisotropy is caused by the SZ effect in galaxy clusters, the method of combining optical and SZ observations should prove to be a powerful technique for identifying galaxy clusters in future SZ surveys. In this first attempt at doing so, we have not modeled the expected optical cluster signature sufficiently to say what constraints this null result places on the role of SZ clusters in producing the observed excess power. There also remains the possibility that anisotropy from galaxy clusters at redshifts beyond the sensitivity of the optical data, $z > 1$, could be contributing significantly to the observed signal in the BIMA survey.

6. CONCLUSION

In this paper, we report the final results from our search for arcminute scale CMB anisotropy using the BIMA array. Modeling the observed power spectrum with a single flat band power with average multipole of $\ell_{eff} = 6864$, we find $\Delta T^2 = 170^{+120}_{-100}\,\mu\text{K}^2$ at 68% confidence and a detection of $\Delta T^2 > 0$ at 92.3% confidence. Dividing the data into two bins corresponding to different spatial resolutions in the power spectrum, we find $\Delta T_1^2 = 220^{+140}_{-120}\,\mu\text{K}^2$ at 68% confidence for CMB flat band power described by an average multipole of $\ell_{eff} = 5237$ and $\Delta T_2^2 < 840\,\mu\text{K}^2$ at 95% confidence for $\ell_{eff} = 8748$. We have used VLA observations and various cuts to test for contamination from radio point sources and systematic effects and conclude that it is unlikely that these sources are responsible for the observed signal. If we assume that the measured excess power is due to a background of distant SZ clusters, we can compare its value with that from simulations of large scale structure to place a constraint on the normalization of matter fluctuations, $\sigma_8 = 1.03^{+0.20}_{-0.29}$ at 68% confidence.

In order to try to determine the source of the observed anisotropy power, we have performed an analysis of the BIMA image statistics. We compared the skewness, asymmetry, and outliers of the measured pixel flux distribution with simulations including noise only and noise plus SZ clusters. A statistical analysis of the BIMA survey images found that they were consistent with simulations including a background of SZ clusters, and inconsistent with simulations of instrumental noise alone or

---

[8] Keck Observatory is operated as a scientific partnership among the California Institute of Technology, the University of California and the National Aeronautics and Space Administration. The Observatory was made possible by the generous financial support of the W.M. Keck Foundation.

[9] KPNO is a Division of the National Optical Astronomy Observatory, which is operated by the Association of Universities for Research in Astronomy, Inc. (AURA) under cooperative agreement with the National Science Foundation.

noise plus radio point sources at $1-2\sigma$. Additional Monte Carlo simulations indicate that with approximately four times the time dedicated to the survey, or equivalently four times the correlated bandwidth, the BIMA instrument would achieve the sensitivity to test the hypothesis of SZ clusters as the source of the observed excess power at greater than 99% confidence. Therefore, future dedicated interferometers, such as the Sunyaev-Zel'dovich Array[10], should be able to effectively use image statistics to determine if any observed anisotropy is due to SZ clusters. Finally, we performed a preliminary search for a correlation between red galaxy density and CMB temperature fluctuations. We are currently unable to quantify the significance of the null result, however, we expect that X-ray and optical follow-up will be essential tools for the interpretation of future SZ surveys.

[10] http://astro.uchicago.edu/sza/

REFERENCES

Bond, J.R., Jaffe, A.H., and Knox, L., 2000, ApJ, 533, 19.

Carlstrom, J.E., Holder, G.P., & Reese, E.D. 2002, ARA&A, 40, 643

Dawson, K.S., Holzapfel, W.L., Carlstrom, J.E., Joy, M., LaRoque, S.J., & Reese, E.D. 2001, ApJ, 553, L1.

Dawson, K.S., Holzapfel, W.H., Carlstrom, J.E., Joy, M., LaRoque, S.J., & Reese, E.D., 2002 ApJ, 581, 86.

Dawson, K. 2004, Ph. D. thesis, UC Berkeley.

Goldstein, J.H., Ade, A.R., Bock, J.J., Bond, J.R., Cantaldi, C., Daub, M.D., Holzapfel, W.L., Kuo, C.L., Lange, A.E., Newcomb, M., Peterson. J.B., Pogosyan, D., Ruhl, J., Runyan, M.C., and Torbet, E., 2003, ApJ, 599, 773.

Gladders, M.D. & Yee, H.K.C., 2000 AJ, 121, 2148.

Gnedin, N.Y. & Jaffe, A.H. 2001, ApJ, 551, .

Hinshaw, G., et al. , 2003, ApJS, 148, 195.

Holzapfel, W.L., Carlstrom, J.E., Grego, L., Holder, G., Joy, M., & Reese, E.D. 2000, ApJ, 539, 57.

Komatsu, E. & Seljak, U. 2002, MNRAS, 336, 1256.

Kuo, C.L., Bock, J.J., Daub, M.D., Goldstein, J.H., Holzapfel, W.L., Lange, A.E., Newcomb, M., Peterson, J.B., Ruhl, J., Runyan, M.C., & Torbet, E., 2004, ApJ, 600, 32.

LaRoque, S.J., Joy, M., Carlstrom, J.E., Ebeling, H., Bonamente, M., Dawson, K.S., Edge, A., Holzapfel, W.L., Miller, A.D., Nagai, D., Patel, S.K., & Reese, E.D., 2003, ApJ, 583, 559.

Mason, B.S. et al. , 2003, ApJ, 591, 540.

Oke, J.B., Cohen, J.G., Carr, M., Cromer, J., Dingizian, A., Harris, F.H., Labrecque, S., Lucinio, R., Schaal, W., Epps, H., & Miller, J., 1995, PASP, 107, 3750.

Pearson, T.J., Shepherd, M.C., Taylor, G.B., & Myers, S.T. 1994, BAAS, 185, 0808.

Perna, R. & Di Matteo, T., 2000, ApJ, 542, 68.

Rubino-Martin, J.A.& Sunyaev, R.A., 2003, MNRAS, 344, 155.

Schulz, A.E. & White M., 2003, ApJ, 586, 723.

Sunyaev, R.A. & Zel'dovich, Y.B., 1970, Ap&SS, 7, 3.

Wolfe T., Reed, R., Blouke, M., Boroson, T., Armandroff, T., & Jacoby, G., 1998 SPIE, 487, 3355.